



# Direct measurement of ocean waves velocity field from a single SPOT-5 dataset

Marcello de Michele <sup>a,\*</sup>, Sébastien Leprince <sup>b</sup>, Jérôme Thiébot <sup>a,1</sup>, Daniel Raucoules <sup>a</sup>, Renaud Binet <sup>c</sup>

<sup>a</sup> Bureau de Recherches Géologiques et Minières (BRGM), Service Risques Naturels, 3 Av. C. Guillemin, 45000, Orléans, France

<sup>b</sup> California Institute of Technology, Division of Geological and Planetary Sciences, Pasadena, CA 91125, USA

<sup>c</sup> Commissariat à l'Energie Atomique et aux Energies Alternatives Centre DAM/Île de France, Bruyères le Châtel 91297 Arpajon Cedex France

## ARTICLE INFO

### Article history:

Received 31 May 2011

Received in revised form 24 November 2011

Accepted 22 December 2011

Available online 30 January 2012

### Keywords:

SPOT

Swell

Ocean waves

Velocity field

Image correlation

Space oceanography

La Reunion Island

## ABSTRACT

We present a method based on space-borne optical imagery from the SPOT5 satellite to directly measure the phase velocity fields of ocean waves. The panchromatic and multispectral scenes acquired by SPOT5 the same day on the same area are not strictly superimposable due to the different locations of the CCDs (Charged Coupled Device) in the focal plane of the instrument. In this manuscript, we propose a method that exploits the temporal lag that exists between the panchromatic and multispectral scenes to measure the ocean wave velocity fields. We firstly discuss the principle and the methodology. Then, we apply it offshore La Reunion Island. Finally, we compare and discuss the results against a swell propagation model. Our method is proven reliable and can be immediately extended to other push-broom sensors.

© 2012 Elsevier Inc. All rights reserved.

## 1. Introduction

Ocean waves represent an important oceanographic phenomenon for manifold reasons. For instance, they strongly influence the most superficial water layer where the exchanges and heat transfer between the ocean and the atmosphere take place. Moreover, the ocean swell highly affects coastal areas, being one of the principal agents responsible for coastal erosion. Furthermore, their propagation pattern being affected by shallow bathymetry, ocean wave velocity fields can provide invaluable information about the ocean floor topography at shallow depth.

Traditional swell measurement methods typically employ sensors mounted on buoys or sensors installed at depth to determine ocean state characteristics. These methods are of great precision and allow one to measure the swell parameters on a point-to-point basis and are therefore well adapted to regions where the ocean swell is spatially uniform. However, in coastal areas the ocean wave field is not spatially uniform as it is modified on its arrival at shallow depth by near-shore processes that depend on local bathymetry (shoaling, refraction, breaking, ...). Therefore, it is of primary importance to measure the swell spatial variations. For instance, phenomena such as coastal erosion and marine flooding are highly dependent on the local wave characteristics. Since classical

in situ instruments are often difficult to deploy in shallow water where waves break, wave models are often used to estimate the local sea state from the offshore wave buoys data. Space-borne imagery has been demonstrated complementary to in-situ measurements in overcoming some of the aforementioned limitations and it typically renders the ocean swell using two frequency bands of the electromagnetic spectrum, the microwave and the visible bands (e.g. Larouche & Lavoie, 1996). The microwave imaging technique consists in an active hyper-frequency system such as the Synthetic Aperture Radar (SAR). The SAR backscattered signal on the ocean surface is dominantly governed by Bragg scattering (e.g. Chapron et al., 2005; Plant & Keller, 1990; Thompson et al., 1991) so that it is the small scale ocean roughness, essentially driven by the wind, that allows for imaging of the ocean swell by radar. A large number of studies have demonstrated that SAR imaging systems are able to correctly evaluate the swell wavelengths and directions even though a certain number of conditions have to be respected for a SAR to image the ocean swell (e.g. Ardhuin et al., 2004; Beal et al., 1983; Breivik et al., 1998; Collard et al., 2005; Dobson & Vachon, 1994). Concretely, most of the aforementioned methods are based on the evaluation of swell spectra retrieved from the SAR imaging systems, not from direct measurements of the swell velocity field. To overcome this limitation, Chapron et al. (2005, 2004) evaluated the Doppler shift of radar echoes occurring during the synthetic aperture as a direct measurement of ocean surface wave velocity (e.g. Johannessen et al., 2008). Since the Doppler shift is analysed on a sub-aperture base, Doppler velocities are obtained at spatial resolutions of 2 km for a narrow swath SAR,

\* Corresponding author. Tel.: +33 238643795; fax: +33 238643689.

E-mail address: [m.demichelle@brgm.fr](mailto:m.demichelle@brgm.fr) (M. de Michele).

<sup>1</sup> Now at Université de Caen, Laboratoire Universitaire des Sciences Appliquées de Cherbourg, 50130 Octeville, France.

and this pioneering method does not yet yield spatially detailed information close to the coast. Higher spatial resolution systems or space-borne Along-Track Interferometry (ATI) might overcome this SAR limitation.

Techniques based on space-borne sensors operating in the visible range of the electromagnetic spectrum capture the specular reflection of visible sunlight on the multiple facets of the ocean swell. These techniques are limited by clouds, and to periods for which the sun, the sensor, and the ocean wave field are in a favourable alignment to allow for the swell image formation. For these reasons, optical techniques have encountered a limited development compared to SAR methods. Still, a large number of studies have demonstrated the potential operational use of optical imaging systems for studying the ocean swell spectra from high resolution SPOT images (e.g. Populus et al., 1991) or for direct measurement of advective surface velocities from medium resolution satellite sensors such as AVHRR, MODIS (e.g. Crocker et al., 2007; Emery et al., 1986) and Nimbus 7 (Garcia & Robinson, 1989). Moreover, a number of studies have demonstrated the potential of airborne infra-red remote sensing to evaluate swell spectra (e.g. Dugan et al., 1996; Gelpi et al., 2001) and surface currents using airborne visible image time series (e.g. Dugan & Piotrowski, 2003). Nonetheless, the direct measurement of ocean wave velocity fields from high resolution visible space-borne imagery is still a challenge.

In this manuscript, we propose an innovative space-based method that jointly uses the panchromatic and multispectral instruments on-board the SPOT-5 satellite, respectively at 5 m and 10 m ground sampling distance (GSD), to directly measure the ocean surface velocity field at very high spatial resolution. Our method relies on two observations. First, owing to the SPOT-5 sensor's geometry, there exists a small temporal lag between “simultaneous” panchromatic and multispectral acquisitions. Because of this temporal lag, moving objects within the scene will therefore be imaged at different locations between panchromatic and multispectral images. Second, the relative displacement of objects between scenes can be measured with high accuracy and precision with well-established image cross-correlation techniques. We present the general concept of the method, test it, and discuss the results by comparing them with modelled ocean swell velocity offshore La Reunion Island (Indian Ocean). We conclude that our method is proven reliable and could be extended to most other space-borne optical sensors to increase temporal data sampling.

## 2. Geometry of the SPOT-5 panchromatic and multispectral sensors

Since 1986, SPOT satellites (SPOT 1–5) have been forming a constellation acquiring images of the Earth from a sun-synchronous near-polar, 832 km altitude orbit with 26 days repeat cycle. SPOT orbits and station positioning are precisely determined by the Doppler Orbitography and Radiopositioning Integrated by Satellite (DORIS) instrument hosted by the payload. The DORIS integrated system allows for the precise computation of SPOT position and velocity every 30 s. In particular, SPOT-5, launched in 2002, is continuously controlled in yaw steering mode by a programmed control loop and a star tracking unit that computes absolute angles along the three attitude axis and provides high accuracy attitude measures to the ground (Riazanoff, 2002). Among other imaging sensors, SPOT-5 is equipped with High Resolution Geometry (HRG1–2) instruments that acquire data in multispectral mode (XS1–2–3) at 10 m spatial resolution and in panchromatic mode (HMA-B) at 5 m GSD respectively. The panchromatic and multispectral scenes acquired the same day on the same area and by the same instrument are not strictly superimposable due to the different locations of the CCDs in the focal plane of the instrument. In particular, an image line acquired at a given time by one of the HRG instruments is approximately  $9.24 \times 10^{-3}$  rad in front of the

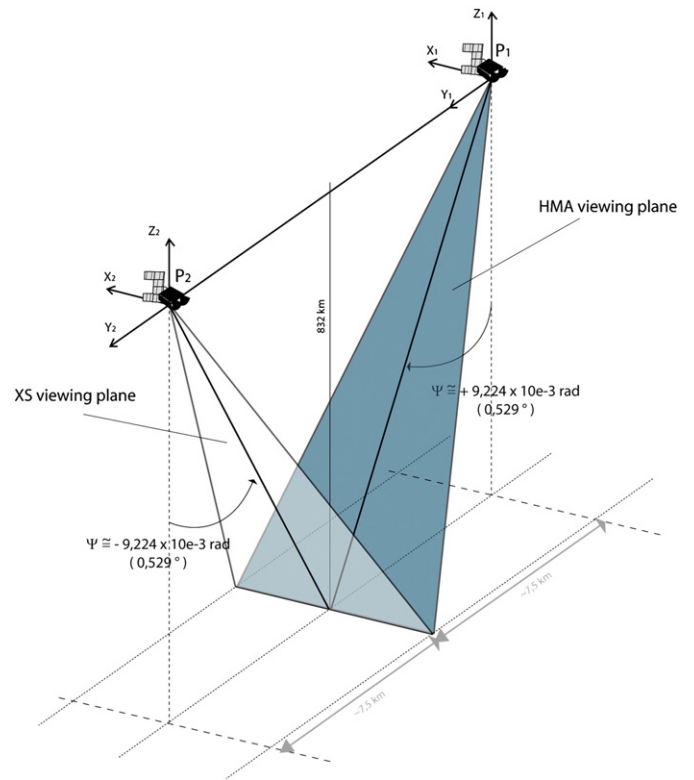


**Fig. 1.** Acquisition geometry of SPOT5 HRG instrument (modified by the authors after Riazanoff, 2002). X, Y and Z represent the attitude state vectors stored in the ancillary data files; P<sub>1</sub> and P<sub>2</sub> indicate the position of the platform at T<sub>0</sub> and T<sub>0</sub> + Δt, when acquiring the HMA and XS data respectively. In this case study, Δt = 2.04 s.

subsatellite point in panchromatic mode (HMA) and  $9.24 \times 10^{-3}$  rad behind the sub-satellite point in multispectral mode (HS) (Fig. 1). This configuration has been exploited to extract Digital Elevation Models (DEM) as it gives rise to a slight parallax view (e.g. Mai & Latry, 2009; Massonnet et al., 1997; Vadon, 2003). Because the sensors are aimed at imaging exactly the same area on the ground, the panchromatic and multispectral scenes are therefore acquired with a temporal shift. For a given SPOT-5 dataset, the platform velocity vector is stored in the ancillary data file. In the case presented here, the imaging ground velocity is then  $\sim 7.53$  km/s. If the platform is flying at a nominal 832 km altitude, it thus takes  $\sim 2.04$  s to cross  $18.48 \times 10^{-3}$  rad ( $\sim 15.37$  km) considering that the Earth curvature is negligible over this distance. Therefore, considering a locally flat surface, if a cluster of pixels, i.e. the ocean waves, within the dataset has moved between the HMA and HS acquisitions, we can measure its velocity by measuring its pixel offset and dividing it by the time lapse between the acquisitions.

## 3. Processing methodology

The conditions for light reflection on the water surface and the SPOT image formation over the ocean have been extensively described by Populus et al. (1991). In the presence of ocean waves higher than 1 m, the sun light reflected by the ocean wave slopes produces glints on the image according to the relative positions between the sensor, the wave front geometry, and the Sun azimuth and elevation. In principle, ocean wave propagation does not produce horizontal displacements of the medium. But given a fixed Sun-wave-sensor geometry, as the waves propagate, the sun-light will produce a glint on the slope of the waves that are in different positions (Fig. 2). Here we start from a set of two SPOT-5 scenes acquired 2.04 s apart (Fig. 3) and use the subpixel phase

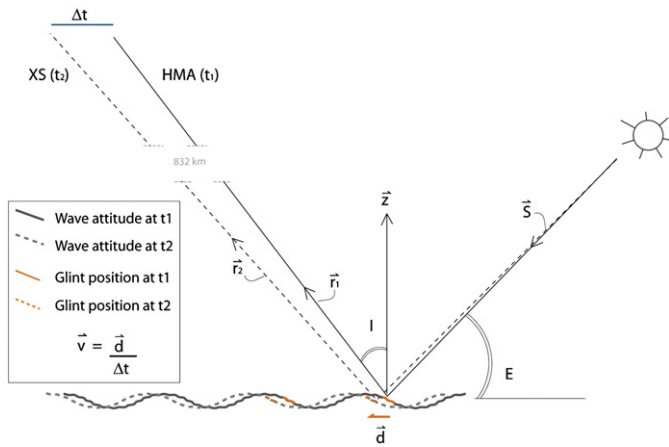


**Fig. 2.** Simplified representation of the glint tracking principle. The Sun light reflected and scattered from the wave slope is recorded by the sensor as glints and different shades of grey. In principle, a wave passing through a medium does not displace matter horizontally, but as glints form for a given Sun-wave-sensor geometry, the glints stick to the wave slope as it moves. Therefore, by measuring the glint offsets (vector “ $d$ ”) and dividing it by image acquisition time lag  $\Delta t$ , we can measure the waves velocity. “ $S$ ” is the sunlight front,  $r_1$  and  $r_2$  are the specular reflections captured by the HMA and HS sensors at times 1 and 2 respectively. Specular reflections are symmetrical to the incident light with the respect to the local surface normal (corresponding to “ $z$ ” in this simplified case). “ $E$ ” is the Sun elevation angle (measured from the horizon) and “ $I$ ” is the viewing incidence with respect to the vertical “ $z$ ”. The condition to get proper surface illumination, is approximately  $60^\circ < E + I < 120^\circ$ . The reader should refer to Populus et al. (1991) for more details.

correlation technique implemented in the COSI-Corr software package (Leprince et al., 2007) to track the glint over time, therefore measuring the phase velocity field of ocean waves.

### 3.1. Dataset

We use a panchromatic + multispectral SPOT-5 dataset acquired over La Reunion Island on February 6th, 2010 (Fig. 2). In particular, we use the HMA panchromatic band with spectral bandwidth centred at  $0.58 \mu\text{m}$ , and analyse it against the XS1 multispectral band (green), which has its spectral bandwidth centred at  $0.55 \mu\text{m}$ . We selected the XS1 because it is the one that closely matches the response of the panchromatic sensor, which can be critical to obtain good image cross-correlation (e.g., Necsoiu et al., 2009). The SPOT-5 orthorectified dataset has been made available in the frame of the Kalideos Project led by the French Space Agency (Centre Nationale d’Etudes Spatiales – CNES). The forward (HRG) and backward (HS) dataset were precisely orthorectified using a rigorous sensor model and a Digital Elevation Model (DEM) by CNES. The HRG and HS dataset are co-registered inland to subpixel accuracy. We subsample the HMA band spatial resolution (5 m) to match the HS spatial resolution (10 m). Then, we use the COSI-Corr correlation to derive the relative pixel offset field that is expected from the ocean wave motion.

### 3.2. Optical image correlation

Image correlation techniques using sliding windows have already been successfully applied to both satellite and airborne photographs to monitor Earth surface displacements. In particular, on seismogenic faults (e.g. Binet & Bollinger, 2005; de Michele et al., 2008; Dominguez et al., 2003; Klinger et al., 2006; Michel & Avouac, 2002, 2006; Van Puymbroeck et al., 2000), on volcano deformation (de Michele & Briole, 2007; Tobita et al., 2001), on gravitational movements assessment (e.g. Berthier et al., 2005; Crippen, 1992; Debella-Gilo & Kaab,

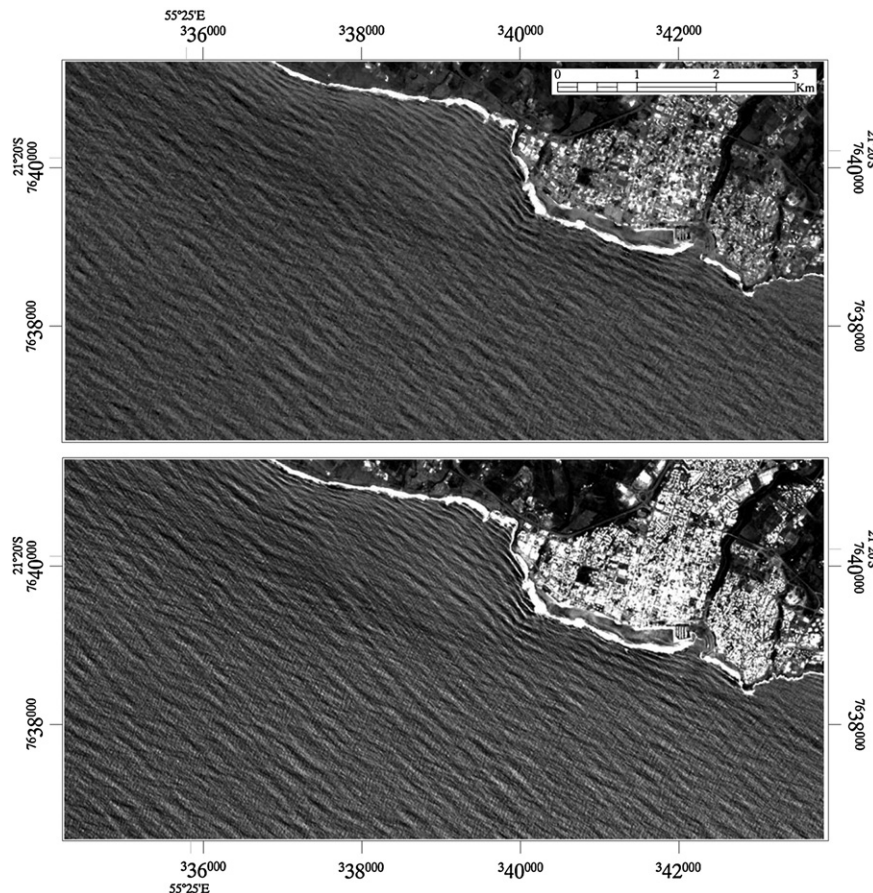


**Fig. 3.** SPOT5 HRG dataset, south of La Reunion Island. Top: the HMA image (subsampled to the 10 m resolution XS image). Bottom: the XS image. We can observe a signal due to the SW/NE swell as well as a higher frequency wind waves directing SE-NW.



2011; Delacourt et al., 2004; Scherler et al., 2008), on sand dunes migration (Necsoiu et al., 2009). This technique analyses the phase difference of the local instantaneous frequency of the images to determine local subpixel offset vectors to a nominal precision better than 1/10 of the pixel size. In this study, we propose to enlarge the spectrum of applications of this method by applying it for the first time to a SPOT5 dataset to measure directly the phase velocity field of ocean waves. The reader should refer to the work of Van Puymbroeck et al. (2000) and to the work of Leprince et al. (2007) for details on the principles of the correlation. In this study, we use a  $64 \times 64$  sliding window with a sampling step of 32 pixels (320 m). We only retain reliable offset measurements, i.e., with a confidence higher than 0.97 as defined by the COSI-Corr correlation signal-to-noise ratio.

### 3.3. Detection limits

Since a parallax view leads to a stereoscopically-driven pixel offsets on regions with varying topography, the parallax between panchromatic and multi-spectral acquisitions is the main potential source of bias to the velocity measurements. The base to height ratio (B/H) controls the sensitivity of a particular acquisition system to the topography, where the base B is the linear distance between the scenes acquisition points and H is the platform altitude. The system configuration presented here yields a B/H equal to 0.018. Hence, the potential bias  $d$ , induced by ocean surface topography  $h$  on the wave offsets is:

$$d = h * (B/H)$$

This means that a potential 10 m high ocean wave (or 10 m error on the DEM) would produce an apparent pixel offset of 0.18 m on a SPOT-5 dataset, which would lead to an apparent wave velocity bias of 0.08 m/s. This is small in comparison to typical wave velocity values ( $\sim 10$  m/s). Moreover, as the epipolar direction may be approximated by the platform velocity direction (along-track stereo), the stereoscopic parallax would induce an error only in the North/South velocity estimates. In summary, we can conclude that the sea surface elevation induced by the waves negligibly influences the accuracy of the ocean wave velocity measurements.

Ocean pixels are correlated by considering that land features are fixed reference points. We verify that the dataset are co-registered to subpixel precision inland by looking at the COSI-Corr correlation score along the coast. Inland, we found a mean of 0.04 pixels offset

with a standard deviation of 0.75 pixels, equivalent to an intrinsic precision on the velocity measures of  $\pm 3.6$  m/s.

SPOT5 is a pushbroom system for which a linear CCD array integrates the sunlight coming from the ground, the line-by-line sampling being performed by the motion of the platform itself perpendicularly to the CCD array. The line-by-line sampling-time is adjusted such that the spatial sampling step is identical in both rows and columns directions. As columns sampling-step is fixed as the distance between two elementary detectors of the CCD projected to the ground, the line-by-line sampling-time to achieve 5 m resolution is nominally 0.75 ms (Latry et al., 2001). Concerning the phenomenon that we aim to measure in this study, we can reasonably consider 0.75 ms per line as an instantaneous sampling which does not significantly influence the wave velocity measurements. Nevertheless, as it takes  $\sim 9$  s to collect the whole 12,000 line HMA dataset, one should consider the aforementioned characteristic when measuring the velocity field of very large scale and fast moving phenomena, such as tsunamis for instance, using the method proposed here.

## 4. Modelling with SWAN

We compare our SPOT-5 velocity field with the velocity field derived with the SWAN wave propagation model. SWAN solves the transport equation for wave energy density (Booij et al., 1999; Ris et al., 1999) and is commonly used to obtain realistic estimates of wave parameters in coastal areas. In our configuration, SWAN simulates the following physical phenomena: wave propagation, shoaling, refraction due to depth, wind effects, and wave energy dissipation by bottom friction and by depth-induced breaking. Our SWAN configuration is nested within the global wave model NOAA WaveWatchIII (Tolman, 1991, 2009). We have used a standard parameterisation which has been validated at La Reunion Island site using data collected at two omnidirectional wavebuoys. In this study, for the comparison with the SPOT-5 data, the results are extracted over a  $1 \times 1$  km grid centred on the study area.

### 4.1. Swell and wind-generated waves: spectral analysis

The ocean surface wave field can be seen as the sum of several harmonic waves. On the SPOT-5 images studied here, we visually distinguish two components of the ocean wave field. On the one hand, we can observe the South-West swell. On the other hand, we can observe a higher frequency wind waves signal directing SE–NW (Fig. 3). Our cross-correlation method measures the amplitudes and the

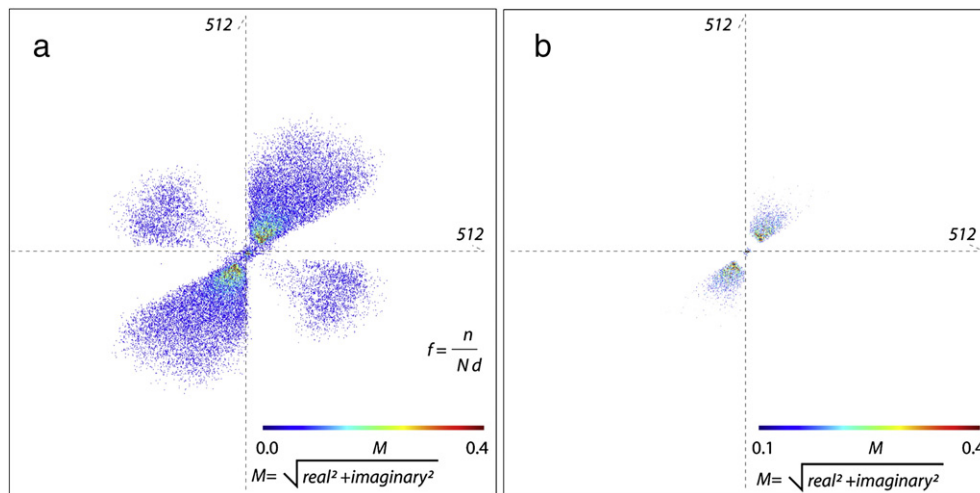


**Fig. 4.** FFT spectrum calculated on a  $512 \times 512$  pixels window over the ocean image. A: FFT spectrum before the filtering. We can clearly see two preferential directions related to the swell (SW–NE) and the wind waves (SE–NW). B: FFT spectrum after filtering. We set the filter in such a way that FFT magnitudes less than 0.1 are discarded and only directions in the 1st and 3rd quadrants are retained for further processing.

directions of the pixel offset vectors resulting from the superposition of these two wave fronts, as they move simultaneously in different directions. These two components of the wave field are clearly visible in the image spectrum (Fig. 4a) calculated over the ocean only.

The modelling with SWAN is based on the distribution of wave energy, which depends on the wave heights, as a function of frequency and direction. Therefore, the spectral discretization in SWAN is different than the one used for retrieving the waves velocity field from SPOT-5. The SWAN wave spectrum highlights the presence of two types of waves: the swell waves and the wind waves, the swell waves being the most energetic. We have restricted the SPOT-5/SWAN data comparison to one type of wave only, the swell. In this case study, as the swell and the wind waves present very distinct propagation directions, we can separate them by applying a directional filter to each of the SPOT 5 images to only retain the information from the swell (Fig. 4b). The filter masks out the values aligned on the frequency axes  $-25/+155$  with a fan of  $40^\circ$ . We also decide to only work with high energy values in the FFT spectrum of Fig. 4a. Practically we filter out all the values within the quadrants 2 and 4 of the FFT spectrum and work with FFT magnitudes higher than 0.1 (i.e., a frequency mask of 0.57 in COSI-Corr). Concerning the results of SWAN, as the swell is more energetic than the wind waves, we use peak parameters (i.e. the sea state parameters calculated where the spectral energy is maximum) to focus on the swell characteristics for the comparison.

## 5. Results

Using subpixel cross-correlation between two SPOT images, we have derived both the velocity field due to the ocean swell alone, and the total velocity field comprised of both swell and wind components. The results in Fig. 5 show that the swell velocity retrieved by SPOT-5 reaches up to 12.9 m/s (2.63 maximum pixels offset) and presents a SW/NE direction. We observe that the results obtained by filtering the SPOT-5 prior to correlation to retain only the swell information closely match the characteristics of the swell calculated with SWAN.

We compute the measurements bias as the norm of the mean difference between SPOT-5 swell velocity vectors and SWAN-modelled swell velocity vectors. Moreover, we assessed the norm of the standard deviation of the X and Y components of the difference vectors. We find a bias of 2.3 m/s (0.4 pixels offset) and a precision of 1.6 m/s (0.3 pixels offset), which correspond to a 25% bias and 17% of misfit

on the SPOT-5 velocity measurements. Considering the direction, we report  $5^\circ$  of standard deviation between SWAN and SPOT results. This value falls within the commonly expected wave directional spreading which is usually between  $10^\circ$  and  $30^\circ$ . Therefore, we can say that this first order comparison yields promising results. The reader should note that there are mainly two caveats to this quantitative comparison. First, the model does not represent the ground truth but the physics of wave propagation based on independently measured inputs. Second, we compare instantaneous measurements vectors from SPOT-5 to time-averaged vectors from SWAN.

## 6. Conclusions and perspectives

In this manuscript, we presented the potential of SPOT imagery for the direct measurement of ocean wave velocity fields. We compared the SPOT-5 results with SWAN modelling, and both methods indicate that the sea state comprises two types of wave regimes: the swell and the wind sea. Focussing on the swell only, the comparison indicates that our methodology is promising. Nevertheless, there are few caveats to the data comparison. Indeed, we have distinguished wind waves from swell waves using a directional criterion but in situations where wind waves and swell waves have similar directions, one should consider alternative filtering methods or account for both phenomena into the modelling. Additional validation is needed in particular in areas where ground instrumentation is dense and data sampling is frequent.

Our methodology is complementary to other space-borne techniques such as the SAR Doppler velocity and could be of great interest particularly to monitor coastal processes. Our approach can directly be extended to archived dataset (e.g. from the whole SPOT archive) to study past phenomena related to ocean circulation. This method could be potentially applied to measure the dynamics of a variety of fast moving phenomena such as ocean eddies, river flows, lava flows, volcanic plumes, tornadoes and hurricanes, icebergs, and glacier flow. The major limitation of this method is related to the image acquisition when the cloud coverage is high. Nevertheless, the revisit time can be improved as the methodology presented here can immediately be extended to the many space-borne push-broom platforms equipped with along-track stereoscopic or multi-spectral sensing capabilities such as ASTER (Kääb & Prowse, 2011; Matthews, 2005; Matthews & Awaji, 2010), PRISM, SPOT-HRS, Quickbird, IKONOS, or Worldview instruments. We encourage detailed investigations on the potential use of those instruments for velocity

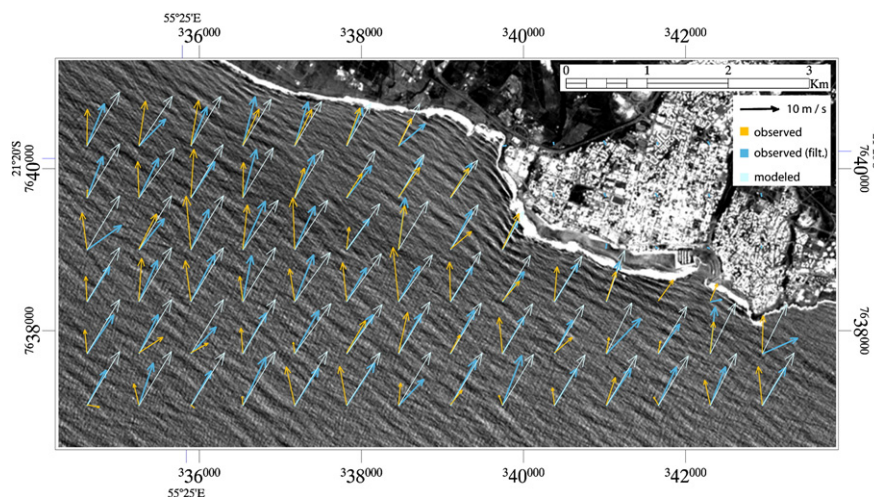


**Fig. 5.** Wave velocity field retrieved from the SPOT-5 dataset (both filtered and not filtered) compared to SWAN modelled results. Orange arrows: velocity vectors obtained from COSI-Corr analysis on non-filtered SPOT-5 data. They represent the velocity field that result from both the swell and the wind waves motion. Dark blue arrows: velocity vectors obtained from COSI-Corr analysis on filtered SPOT-5 data. These vectors reasonably correspond to swell velocity field. Light blue arrows: velocity vectors obtained from SWAN swell analysis.

field measurements and recommend this data acquisition configuration for future missions.

## Acknowledgements

We thank the Kalideos team (CNES) for providing the SPOT5 dataset. Discussions with Alain Giros improved the manuscript. We are thankful to Nadia Khezami for her earlier inputs to this study. MdM, JT, DR thank BRGM Research Direction for supporting the study. SL was partly supported by the Keck Institute for Space Study and by the Gordon and Betty Moore Foundation.

## References

- Ardhuin, F., Collard, F., & Chapron, B. (2004). Wave spectra from ENVISAT's Synthetic Aperture Radar in coastal areas. *Proceedings of the 14th (2004) International Off-shore and Polar Engineering Conference*, Toulon, France, May 23–28.
- Beal, R. C., Tilley, D. G., & Monaldo, F. M. (1983). Large and small scale spatial evolution of digitally processed ocean wave spectra from SEASAT Synthetic Aperture Radar. *Journal of Geophysical Research*, 88, 1761–1778.
- Berthier, E., Vadon, H., Baratoux, D., Arnaud, A., Vincent, C., Feigl, K. L., Rémi, F., & Legrésy, B. (2005). Surface motion of mountain glaciers derived from satellite optical imagery. *Remote Sensing of Environment*, 95, 14–28.
- Binet, R., & Bollinger, L. (2005). Horizontal coseismic deformation of the 2003 Bam (Iran) earthquake measured from SPOT-5 THR satellite imagery. *Geophysical Research Letters*, 32(2), doi:10.1029/2004GL021897.
- Booij, N., Ris, R. C., & Holthuijsen, L. H. (1999). A third-generation wave model for coastal regions, Part I, Model description and validation. *Journal of Geophysical Research*, 104(C4), 7649–7666.
- Breivik, L. A., Reistad, M., Schyberg, H., Sunde, J., Krogstad, H., & Johnsen, H. (1998). Assimilation of ERS SAR wave spectra in an operational wave model. *Journal of Geophysical Research*, 103(C4), 7887–7900.
- Chapron, B., Collard, F., & Ardhuin, F. (2005). Direct measurements of ocean surface velocity from space: Interpretation and validation. *Journal of Geophysical Research*, 110, doi:10.1029/2004JC002809.
- Chapron, B., Collard, F., & Kerbaol, V. (2004). Satellite Synthetic Aperture Radar sea surface Doppler measurements. *Proceedings of 2nd Workshop on Coastal and Marine Applications of Synthetic Aperture Radar, esa sp-565* (pp. 133–141). Paris: Eur. Space Agency.
- Collard, F., Ardhuin, F., & Chapron, B. (2005). Extraction of coastal ocean wave fields from SAR images. *IEEE Journal of Oceanic Engineering*, 30(3), 526–533.
- Crippen, R. E. (1992). Measurements of sub resolution terrain displacements using Spot panchromatic imagery. *Episodes*, 15, 56–61.
- Crocker, R. I., Matthews, D. K., Emery, W. J., & Baldwin, D. G. (2007). Computing coastal ocean surface currents from infrared and ocean color satellite imagery. *IEEE Transactions on Geoscience and Remote Sensing*, 45(2).
- de Michele, M., & Briole, P. (2007). Deformation between 1989 and 1997 at Piton de la Fournaise volcano retrieved from correlation of panchromatic airborne images. *Geophysical Journal International*, 169, 357–364, doi:10.1111/j.1365-246X.2006.03307.x.
- de Michele, M., Raucoules, D., Aochi, H., Baghdadi, N., & Carnec, C. (2008). Measuring coseismic deformation on the northern segment of the Bam-Baravat escarpment associated with the 2003 Bam (Iran) earthquake, by correlation of very-high-resolution satellite imagery. *Geophysical Journal International*, 173(2), 459–464.
- Debella-Gilo, M., & Kaab, A. (2011). Sub-pixel precision image matching for measuring surface displacements on mass movements using normalized cross-correlation. *Remote Sensing of Environment*, 115, 130–142.
- Delacourt, C., Allemand, P., Casson, B., & Vadon, H. (2004). Velocity field of « La Clapière » landslide measured by correlation of aerial and Quickbird satellite images. *Geophysical Research Letters*, 31, L15619.
- Dobson, F. W., & Vachon, P. W. (1994). The Grand Banks ERS-1 SAR wave spectra validation experiment: Program overview and data summary. *Atmosphere-Ocean*, 32(1), 7–29.
- Dominguez, S., Avouac, J. P., & Michel, R. (2003). Horizontal coseismic deformation of the 1999 Chi-Chi earthquake measured from SPOT satellite images: Implications for the seismic cycle along the western foothills of central Taiwan. *Journal of Geophysical Research*, 108(B2), 2083, doi:10.1029/2001JB000951.
- Dugan, J. P., & Piotrowski, C. C. (2003). Surface current measurements using airborne visible image time series. *Remote Sensing of Environment*, 84(2), 309–319.
- Dugan, J. P., Suzukawa, H. H., Forsyth, C. P., & Faber, M. S. (1996). Ocean wave dispersion surface measured with airborne IR imaging systems. *IEEE Transactions on Geoscience and Remote Sensing*, 34(5), 1282–1284.
- Emery, W. J., Thomas, A. C., & Collins, M. J. (1986). An objective method for computing advective surface velocities from sequential infrared satellite images. *Journal of Geophysical Research*, 91(C11), 12,865–12,878.
- Garcia, C. A. E., & Robinson, I. S. (1989). Sea surface velocities in shallow seas extracted from sequential coastal zone color scanner satellite data. *Journal of Geophysical Research*, 94(C9), 12,681–12,691.
- Gelpi, C. G., Shuraytz, B. C., & Husman, M. E. (2001). Ocean wave height spectra computed from high-altitude, optical infrared images. *Journal of Geophysical Research*, 106(C11), 31403–31413.
- Johannessen, J. A., Chapron, B., Collard, F., Kudryavtsev, V., Mouche, A., Akimov, D., & Dagestad, K. F. (2008). Direct ocean surface velocity measurements from space: Improved quantitative interpretation of Envisat ASAR observations. *Geophysical Research Letters*, 35(L22608), doi:10.1029/2008GL035709.
- Kääb, A., & Prowse, T. (2011). Cold-regions river flow observed from space. *Geophysical Research Letters*, 38(L08403), doi:10.1029/2011GL047022.
- Klinger, Y., Michel, R., & King, G. C. P. (2006). Evidence for an earthquake barrier model from Mw ~7.8 Kokoxili (Tibet) earthquake slip distribution. *Earth and Planetary Science Letters*, 242, 354–364.
- Larouche, P., & Lavoie, A. (1996). La télédétection appliquée à l'étude des océans. In F. Bonn (Ed.), *Précis de Télédétection. Application Thématiques*, Vol. 2. (pp. 347–392). Québec: Presses de l'Université du Québec.
- Latry, C., Rougé, B., & Baillarin, S. (2001). La chaîne d'image SPOT5 THR: un exemple d'optimisation globale. 18<sup>e</sup> Colloque sur le traitement du signal et des images, Groupe d'Etudes du Traitement du Signal et des Images (GRETSI), Toulouse, France (pp. 184–187). (in French).
- Leprince, S., Barbot, S., Ayoub, F., & Avouac, J. -P. (2007). Automatic and precise orthorectification, coregistration, and subpixel correlation of satellite images: Application to ground deformation measurements. *IEEE Transactions on Geoscience and Remote Sensing*, 45, 1529–1558.
- Mai, S., & Latry, C. (2009). Digital Elevation Model computation with SPOT5 panchromatic and multispectral images using low stereoscopic angle and geometric model refinement. *Proceedings of the 2009 IEEE International Geoscience and Remote Sensing Symposium*, 12–17 July, Cape Town, South Africa.
- Massonnet, D., Giros, A., & Breton, E. (1997). Forming digital elevation models from single pass Spot data: Results on a test site in the Indian Ocean. *Proceedings of the 1997 IEEE International Geoscience and Remote Sensing Symposium*, 03–08 August, Singapore.
- Matthews, J. (2005). Stereo observation of lakes and coastal zones using ASTER imagery. *Remote Sensing of Environment*, 99, 16–30.
- Matthews, J. P., & Awaji, T. (2010). Synoptic mapping of internal-wave motions and surface currents near the Lombok Strait using the along Track Stereo Sun Glitter technique. *Remote Sensing of Environment*, 114(8), 1765–1776.
- Michel, R., & Avouac, J. P. (2002). Deformation due to the 17 August 1999 Izmit, Turkey, earthquake measured from SPOT images. *Journal of Geophysical Research*, 107(B4), doi:10.1029/2000JB000102.
- Michel, R., & Avouac, J. P. (2006). Coseismic surface deformation from air photos: The Kickapoo step over in the 1992 Landers rupture. *Journal of Geophysical Research*, 111(B03408), doi:10.1029/2005JB003776.
- Necsoiu, M., Leprince, S., Hooper, D. M., Dinwiddie, C. L., McGinnis, R. N., & Walter, G. R. (2009). Monitoring migration rates of active subarctic dune field using optical imagery. *Remote Sensing of Environment*, 113, 2441–2447.
- Plant, W. J., & Keller, W. C. (1990). Evidence of Bragg scattering in microwave Doppler spectra of sea return. *Journal of Geophysical Research*, 95(C9), 16299–16310.
- Populus, J., Aristaghes, C., Jonsson, J. L., Augustin, J. M., & Pouliquen, E. (1991). The use of SPOT data for wave analysis. *Remote Sensing of Environment*, 36, 55–65.
- Riazanoff, S. (2002). *Spot Geometry Handbook*, 74 pages, ed. SPOT-IMAGE, 5 rue des Satellites, 31030 Toulouse Cedex 4, France, January 2002.
- Ris, R. C., Booij, N., & Holthuijsen, L. H. (1999). A third-generation wave model for coastal regions, Part II, Verification. *Journal of Geophysical Research*, 104(C4), 7667–7681.
- Scherler, D., Leprince, S., & Strecker, M. R. (2008). Glacier-surface velocities in alpine terrain from optical satellite imagery – Accuracy improvement and quality assessment. *Remote Sensing of Environment*, 112, 3806–3819.
- Thompson, D. R., Gotwols, B. L., & Keller, W. C. (1991). A comparison of Ku-band Doppler measurements at 20° incidence with predictions from a time-dependent scattering model. *Journal of Geophysical Research*, 96(C3), 4947–4955.
- Tobita, M., Murakami, M., Nakagawa, H., Yara, H., & Rosen, P. A. (2001). 3-D surface deformation of the 2000 Usu eruption measured by matching of SAR images. *Geophysical Research Letters*, 28, 4291–4294.
- Tolman, H. L. (1991). A third-generation model for wind waves on slowly varying, unsteady and inhomogeneous depths and currents. *Journal of Physical Oceanography*, 21, 782–797.
- Tolman, H. L. (2009). User manual and system documentation of WAVEWATCH III version 3.14. NOAA/NWS/NCEP/MMAB technical note, 276, 194 pp.
- Vadon, H. (2003). 3D Navigation over merged Panchromatic-Multispectral high resolution SPOT5 images. *Proceedings of the 2003 ISPRS symposium. The International Archives of the Photogrammetry, Remote Sensing and Spatial Information Sciences*, Vol. XXXVI. (pp. 5/W10).
- Van Puymbroeck, N., Michel, R., Binet, R., Avouac, J. P., & Taboury, J. (2000). Measuring earthquakes from optical satellite images. *Applied Optics*, 39(20), 3486–3494.